2014

Lattice thermal conductivity in bulk and nanosheet NaxCoO2

Denis Demchenko
Virginia Commonwealth University, ddemchenko@vcu.edu

David B. Ameen
Virginia Commonwealth University

Lattice thermal conductivity in bulk and nanosheet Na_xCoO_2

D. O. Demchenko and D. B. Ameen
Department of Physics, Virginia Commonwealth University, Richmond VA 23284

In this paper we present the results of calculations of the lattice thermal conductivity of layered complex metal oxide Na_xCoO_2 within the Green-Kubo theory. Using Na_xCoO_2 we identify the two competing mechanisms responsible for the favorable scaling properties of the Green-Kubo method for calculating the lattice thermal conductivity. The artificial correlations of the heat flux fluctuations due to the finite size of the supercells are partially cancelled by the missing long wavelength acoustic phonon modes. We compute the lattice thermoelectric properties of bulk Na_xCoO_2 with varying stoichiometry, structural defects, and temperature. We also calculate the thermal conductivity of Na_xCoO_2 in the nanosheet geometry. While the dependence of thermal conductivity on Na fractions x in the middle range ($0.5 < x < 0.8$) is relatively weak, introducing Co vacancies results in significant lattice thermal conductivity reduction. The material exhibits strong anisotropy of lattice thermal conductivity due to a layered crystal structure and relatively weak bonding between layers. This structure leads to the possibility of manufacturing relatively large nanosheets of Na_xCoO_2. However, the weak inter-layer binding also results in the insensitivity of thermal conductivity to the nanosheet thickness.

Corresponding author: ddemchenko@vcu.edu; 1-804-828-7077

I. Introduction

Layered complex metal oxide Na_xCoO_2 and its nanostructures are promising materials due to a variety of potential applications. Initial interest has been focused on the battery applications [1,2] as well as superconductivity of its hydrated phase [3,4]. Recently one of the most interesting applications of Na_xCoO_2 has been thermoelectric conversion of heat. Unusually large thermoelectric power in single crystal $NaCo_2O_4$ has been reported [5], showing in plane values of 100 μV/K at 300 K, that in combination with low in-plane resistivity of 200 μ Ωcm at 300 K makes this material a potential competitor of conventional thermoelectric materials such as Bi_2Te_3. Further experiments found a strong dependence of thermopower on an applied magnetic field, suggesting that the spin entropy dominates the enhancement of thermopower [6]. This, however, was disputed when later experiments suggested that the quasiparticle lifetime is affected by the magnetic field and may cause the observed anisotropic magnetic field dependence of the thermoelectric power, indicating that the electronic structure is responsible for the unique combination of large thermoelectric power and metallic electrical conductivity [7,8].

The theoretical analysis of electronic structure of Na_xCoO_2 is complicated by the strongly correlated nature of this material [9,10]. The unusual thermoelectric properties of Na_xCoO_2 have been analyzed theoretically using the many-body theory [11] and density functional theory [12], suggesting that the observed thermopower and specific heat can be explained by the material's band structure, with the enhancement of thermopower possibly due to electronic correlations [13]. Boltzmann transport calculations based on the material's band structure also reasonably agree with measured values of thermopower [14,15].

Structural properties of Na_xCoO_2 have been studied for different Na ratios x by various diffraction methods [16,17,18,19,20,21], revealing several closely related layered structures consisting of layers of shared CoO_6 octahedra, and Na atoms randomly occupying different symmetry sites between layers of cobalt oxide. Density functional theory (DFT) calculations have predicted several ordered structures of Na vacancies within each layer [22]. Lattice properties of Na_xCoO_2 have also been studied by first principles lattice dynamics calculations [23] as well as classical molecular dynamics [24] (MD), producing a phonon spectrum that shows considerable anisotropy with little dependence on Na site occupancy. Lattice thermal conductivity and its dependence on the amounts of Na have been much less studied. Classical molecular dynamics has been used to probe the lattice thermal properties for only two selected ratios of Na [25,26,27]. The details of the lattice thermal conductivity are important for the design of novel thermoelectric materials since the suppression of the lattice component of thermal conductivity is one of the main recipes currently used to boost thermoelectric conversion efficiency.

The layered structure with its strong bond anisotropy leads to the possibility of manufacturing nanosheets of Na_xCoO_2 by chemical exfoliation [28]. Recently a highly efficient scalable exfoliation of $Na_{0.7}CoO_2$ nanosheets has been demonstrated producing samples that are a millimeter in length and 10-100 nm in thickness [29]. The nanostructuring approach to oxide thermoelectric materials [30] relies on introducing phonon scattering surfaces and interfaces in a nanostructure, thereby reducing the lattice thermal conductivity and increasing the thermoelectric figure of merit ZT [31]. This direction is promising for increasing the overall thermoelectric efficiency, although other means of ZT increase should be pursued as well, since nanostructuring alone may not be sufficient to enhance ZT to practical levels [32]. Since such nanoscaling approach is aimed at reducing the lattice part of thermal conductivity, in this paper we focus on the thermoelectric lattice properties of different compositions of Na_xCoO_2, as well as their nanosheets.

II. Methods

Equilibrium molecular dynamics simulations using the Green-Kubo formalism [33,34] are employed to calculate the lattice thermal conductivity κ_L for a series of bulk Na_xCoO_2 with varying Na ratio x as well as its nanosheets, as implemented in LAMMPS (Large-scale Atomic/Molecular Massively Parallel Simulator) [35,36]. The material is represented by a series of supercells of varying sizes with periodic boundary conditions. Since the Green-Kubo method for calculating thermal conductivity requires the bulk material to be in thermodynamic equilibrium, the initial MD simulations are preformed allowing the crystal lattice to relax at the designated temperature. After equilibrium structure and volume are obtained, the calculations are performed in the *NVT* ensemble with Nosé-Hoover thermostat. Upon the initial MD simulation to achieve thermal equilibrium, the heat flux J_x in the x-dimension for a system is calculated through [37]

$$J_x = -\frac{1}{V_0}\sum_i \mathbf{S}_i v_{xi} \,, \tag{1}$$

where V_0 is the equilibrium volume of the crystal, $\mathbf{S}_i$ is the stress tensor for ion i, v_{xi} is the velocity of ion i in the x-dimension, and the convective portion of the heat flux is assumed to be zero. Within the Green-Kubo theory the lattice thermal conductivity is related to the rate of decay of the equilibrium fluctuations of the heat current. Along a direction x the lattice thermal conductivity κ_L can be computed as the integral of the heat current autocorrelation function (ACF)

$$\kappa_x = \frac{V_0}{k_B T^2}\int_0^\infty \langle J_x(0) J_x(t)\rangle dt \,, \tag{2}$$

where k_B is Boltzmann's constant and T is temperature. The brackets denote equilibrium averaging, which is often replaced by time averaging, assuming ergodicity is satisfied. However, the ensemble averaging over random initial conditions is also necessary since in finite systems the ergodicity condition is not usually fulfilled [38]. The ensemble averaged ACF decays to zero with time and therefore produces converged values of the ACF integrals. A

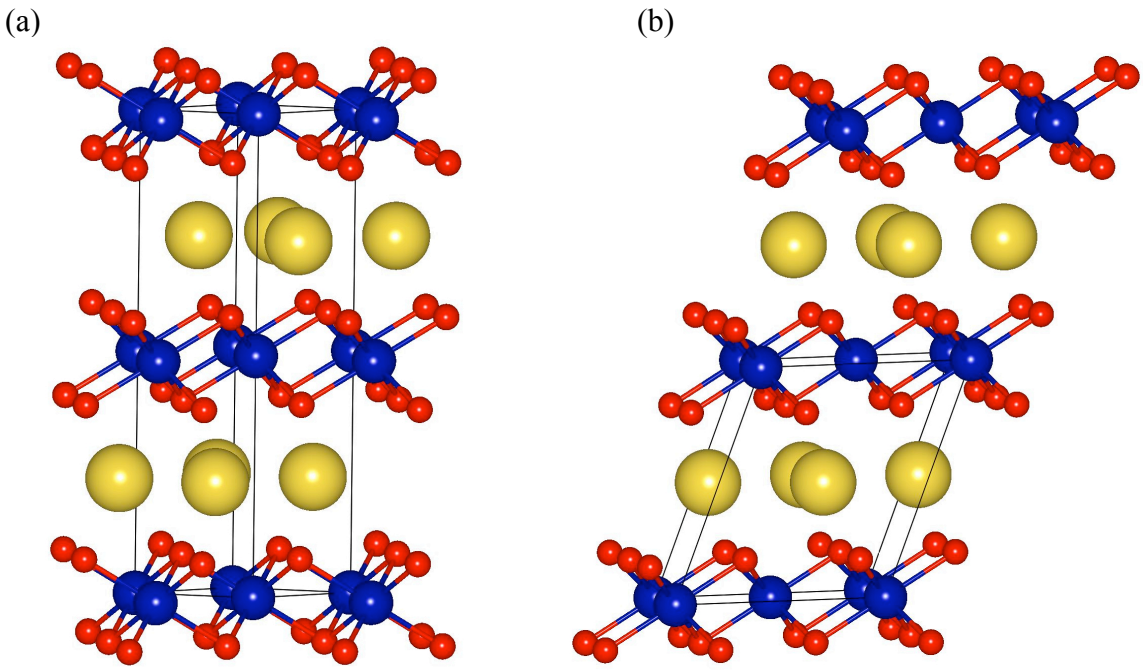

Fig. 1. (Color online) Crystal structures of Na_xCoO_2: (a) two-layer structure (γ-phase) and (b) three-layer structure (related to α- and β-phases). Large yellow atoms represent Na, smaller blue and red atoms are Co and O, respectively.

Gaussian distribution of initial velocities is randomly assigned to the lattice ions for each data run according to a varying input seed value. The results from different initial conditions vary significantly, necessitating the averaging of results over at least nine ensembles to achieve converged results. The equations of motion are integrated with a time step of 0.5 fs and the heat flux statistics are accumulated for 1.6 ns.

The Green-Kubo approach outlined above based on the fluctuation-dissipation theorem, although less intuitive in comparison with the direct non-equilibrium MD (NEMD) method [39], offers some advantages. For example, the entire thermal conductivity tensor can be computed during a single MD run, whereas separate calculations must be performed by NEMD to obtain the thermal conductivities in different directions. In addition, and this is the most important property for the calculations of κ_L in nanostructures, it is much less sensitive to the system size in the direction of heat propagation. It has been reported [38] that in the Green-Kubo method the size conversion is achieved for relatively small supercell sizes due to possible cancellation of certain competing effects, although their exact nature was not identified. In contrast, in the NEMD the nature of phonon transport is partially ballistic and in an ideal crystal can considerably increase the necessary system sizes in the direction of current propagation [40].

Na_xCoO_2 is realized in three closely related crystal structures, labeled in the literature as the α-, β-, and γ-phases. All structures consist of layers of CoO_2, with each Co atom coordinated by six oxygen atoms, as shown in Figure 1. Na atoms are randomly distributed over different symmetry sites in the intervening layers and are weakly bound and therefore highly mobile. The three Na_xCoO_2 structures differ in the stacking sequence of the Co-O layers. In the γ-phase (two layer structure) Co atoms are stacked vertically in series, while in the α- and β-phases (three layer structures) Co atoms in adjacent layers are shifted by 1/3 along the diagonal of the unit cell. These typically have symmetries with space groups *P6₃/mmc* for two-layer structures and *C2/m* for three-layer structure. A series of lattice structures can be obtained with varying Na concentrations within each underlying two- or three-layer structures. For example, the two-layer derived structures of Na_xCoO_2 can be obtained with Na amounts x=0.34, 0.5, 0.63, 0.71, 0.76, 0.80, and 1.0, while three-layer derived structures are observed with Na amounts x=0.32, 0.5, 0.6, 0.67, 0.75, 0.92 [20,21]. Since each basic lattice can accommodate a variety of Na concentrations, in this work we use the more common γ-phase two-layer structure of Na_xCoO_2 (Fig. 1(a)), in order to relate our results to experiments obtained for both bulk [16] and exfoliated nanosheets [29] of $Na_{0.71}CoO_2$. Starting with the ideal γ-phase $NaCoO_2$ structure, we randomly introduce a (1-x) percentage of Na vacancies in the supercells, ensuring an even distribution of vacancies in the sample. In addition, structural characterization experiments have shown a significant amount of Co vacancies (~4%) in both bulk $Na_{0.71}CoO_2$, and exfoliated nanosheets [16,29]. We introduce randomly distributed Co vacancies, in order to explore the influence of Na and Co lattice defects on lattice thermal conductivity, since they could suppress phonon heat transport. The starting lattice parameters used here are a=2.831 Å and c=10.8756 Å in the ideal $Na_{0.71}CoO_2$ structure. In order to eliminate size effects [41], a series of supercells is studied in our size scaling tests with the number of atoms in the supercells varying from 100 to 26,000 (with 6,500 atom cells found to be optimal).

Classical MD runs are performed using the Buckingham potential and include long-rage Coulomb interactions, with

$$\varphi\left(r_{ij}\right) = \frac{q_i q_j}{r_{ij}} + A_{ij}\exp\left(-\frac{r_{ij}}{\rho_{ij}}\right) - \frac{C_{ij}}{r_{ij}^6}. \qquad (3)$$

In the Coulombic term, q_i and q_j are the charges on the i,j ion pair, r_{ij} is the distance between these ions, A_{ij}, ρ_{ij} , and C_{ij}, are the Buckingham potential parameters fitted to represent properties of the bulk material. The charged ions include Na^+, O^{2-}, and $Co^{\alpha+}$. The fractional cobalt ion's charge α (varying from 3.0+ to 3.66+) enables the introduction of varying fractions of Na x as well as Co vacancies (from 0 to 10%) while maintaining the charge neutrality of the bulk material. The short-range interactions characterized by the potential function (3) are represented by the parameters A_{ij}, r_{ij}, and C_{ij}, as taken from Ref. 27. These parameters were originally obtained from the *ab-initio* calculations, and are applied only to the Na^+-O^{2-}, $Co^{\alpha+}$–O^{2-}, and O^{2-}–O^{2-} pairs. Since in Ref. 27 the reported parameters are for Co^{3+} and Co^{4+}, in the present study we use linear interpolation of these parameters to obtain those for $Co^{\alpha+}$. Consistent with the previous studies [25,26], only the Coulombic term is considered for the three metal-metal interactions, which include Na^+–Na^+, $Co^{\alpha+}$–$Co^{\alpha+}$, and Na^+–$Co^{\alpha+}$. The general potential parameters reported by Cherry *et al*. [42] are used for the O^{2-}–O^{2-} interactions. In order to achieve greater accuracy regarding long-range electrostatic interactions, these are calculated in reciprocal space using an Ewald-type summation. The cut-off radii in real space for the Buckingham type interactions and for the short-range Coulomb interactions are 7.0 Å and 12.0 Å, respectively.

Prior to the heat flux ACF calculations, we confirm the transferability of the potentials provided in Ref. 27 to the present study's bulk model by comparison of the MD simulation lattice and elastic constants to those found in the literature. The present study is different from the model used to derive the potentials in the following ways: (1) use of a sodium fraction that varies from 0.30 to 1.00 (rather than fixed at 1.00 or 0.50); (2) use of cobalt vacancies so that the cobalt fraction varies from 0.90 to 1.00 (rather than being fixed at 1.00); and (3) use of a single cobalt ion charge α rather than an alternating +3/+4 ion charge assignment in different layers. In the present MD simulation the 1600 atom supercell is used to determine the equilibrium lattice constants by relaxing the lattice in the *NPT* ensemble. The resultant lattice constant values show good agreement with the experimental values [16,43] obtained for $Na_{0.75}CoO_2$ (Table I). Elastic constants are determined from the MD simulations by fitting the potential energy of the system in equilibrium at room temperature into a quadratic expression with respect to the applied strain that assumes an elastic crystal deformation. The resultant elastic constants obtained here show good agreement with the results obtained in Ref. 27, using a linear interpolation between the values that they calculated for $Na_{0.5}CoO_2$ and $NaCoO_2$ (Table I). This suggests that the assignment of the fractional charge to Co ions in relatively large supercells produces results comparable to the published data.

TABLE I. Comparison of lattice constants a [Å] and c [Å] and elastic constants C_{11} [GPa] and C_{33} [GPa] for $Na_{0.75}CoO_2$ between present study and results found in literature

Source	a	c	C_{11}	C_{33}
MD simulation (present study)	2.875	10.97	467	150
Experiment[a]	2.833	10.88		
Experiment[b]	2.839	10.99		
MD simulation[c]			482	165

[a]Fouassier *et al.*[16]
[b]Seetawan *et al.*[43]
[c]Linear interpolation between the results for $Na_{0.5}CoO_2$ and $NaCoO_2$[27]

III. Results and Discussions

3.1 Auto-Correlation Function

The indirect nature of the Green-Kubo method of calculating lattice thermal conductivity κ_L leads to features in the ACF that require careful analysis in order to obtain converged results. One consequence of the ACF behavior in supercells with periodic boundary conditions is the competition between spurious inflation and reduction of κ_L, which becomes more significant as crystal size is reduced. The general behavior of the ACF of heat flux J_x (as defined in Eq. 1) in a solid is an oscillating function with a decaying exponential envelope

$$\left\langle J_x(0)J_x(t)\right\rangle = I_0 e^{-\beta t}\cos(\omega t), \tag{4}$$

where I_0 is the ACF initial value and β is the time decay constant. The integral of Eq. (4) shows that κ_L is proportional to the ratio I_0/β, with β being the factor that introduces the false inflation of κ_L, while I_0 causes false reduction of κ_L as crystal size is reduced. Within the Green-Kubo formalism the amount of heat propagated in a given direction is related to the rate of the energy dissipation by fluctuations in the system. The correlations between these fluctuations reveal acoustic phonon modes capable of transferring heat. The resulting magnitude of the lattice thermal conductivity is thus dependent on the number of available acoustic phonon modes. As the crystal size is reduced, the number of long wavelength phonon modes capable of carrying heat is reduced, decreasing the magnitude of the heat flux. This leads to the reduced values of I_0, and lower values of the ACF integral. On the other hand, reduction of the supercell size leads to the longer energy relaxation times by introducing spurious fluctuation correlations of the heat flux, leading to the longer decay tails in ACF. This causes the heat flux correlations to persist for a longer period of time, reducing the time decay constant β, and extending the integral tail. The longer correlation time leads to a higher calculated κ_L. Because of these two competing effects on thermal conductivity it is necessary to monitor the scaling of κ_L with crystal size to determine when κ_L has converged, i.e., when the I_0/β ratio becomes constant. This is particularly crucial when doing temperature dependent calculations of κ_L, since these competing effects change at different rates with varying temperature. It has been suggested in the literature (detailed

analysis can be found in Ref. 38) that due to this partial cancellation of the two competing effects, the Green-Kubo method offers relatively quick convergence with respect to supercell size.

Figure 2 demonstrates the cancellation of the two competing contributions to κ_L as discussed above. Typical examples of normalized ACF functions calculated for $Na_{0.71}Co_{0.96}O_2$ are shown in Figure 2, where a portion of the ACF decay from 1.5 ps to 3 ps is shown. The size effect on the ACF is shown by varying the supercell size in the direction of the computed lattice thermal conductivity that is perpendicular to the CoO_2 layers. The supercell thicknesses are 21.9 Å, 43.9 Å, and 65.8 Å. For the smallest supercell with L_Z= 21.9 Å, the ACF is clearly not zero at 3 ps, leading to a longer ACF decay tail and a larger contribution to κ_L. On the other hand, as shown by the inset (a) to Figure 2, which plots the initial values of the ACF (normalized to a single maximum), there is a decrease in the ACF with decreasing size. Although these differences appear small, obscured by the large amplitude oscillations in ACF, the value of an integral is strongly affected by them. Overall the goal is to achieve convergence with respect to both effects. As evident from Figure 2, the ensemble averaged ACF for a larger (L_Z= 43.9 Å, and L_Z= 65.8 Å) supercell sizes approaches zero beyond 3 ps, and there is an incremental increase in the ACF amplitude with increasing supercell size from 43.9 Å to L_Z= 65.8 Å, indicating well converged values of the ACF integrals.

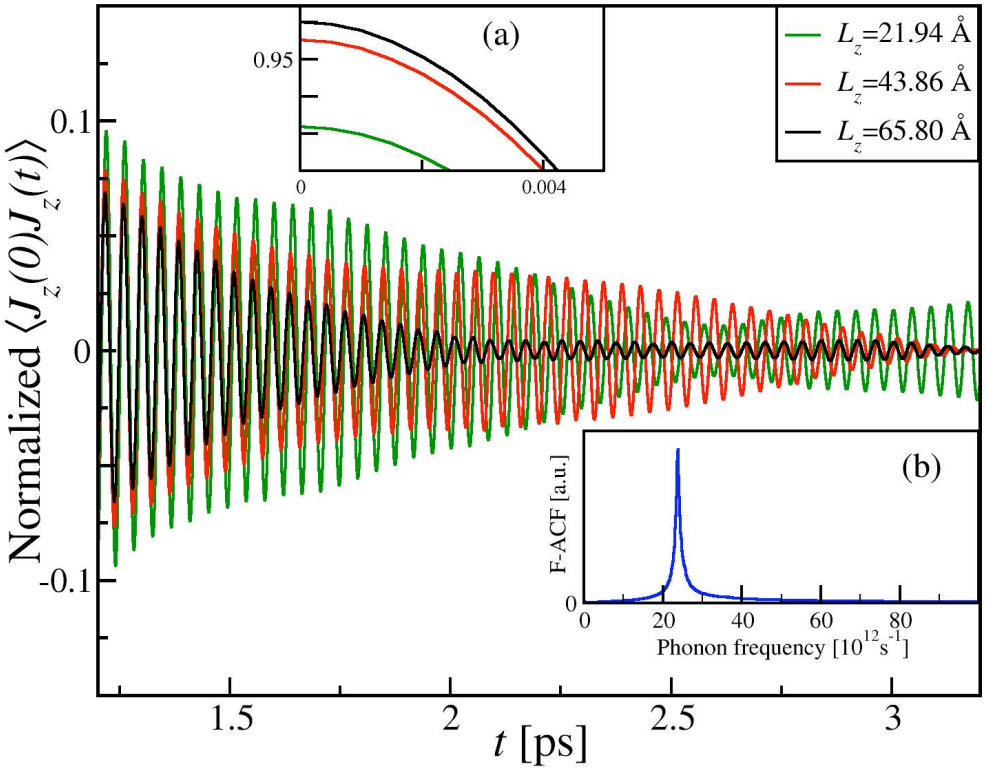

Fig. 2. (Color online) Heat flux auto-correlation function (ACF) computed for $Na_{x0.71}Co_{0.96}O_2$ at room temperature for three different supercell sizes. The tail of the ACF is shown after ~1.4 ps to demonstrate the differences in ACF with supercell size. Inset (a) shows the initial (in the vicinity of t=0) values of the ACF for the three different sizes of the ACF. Inset (b) shows the Fourier transform of the ACF.

The structure of the ACF in Figure 2 also shows the exponential envelope of the ACF originating from the fluctuation dissipating heat flux correlations, as well as the periodic part of the ACF caused by the Γ-point optical phonons. Similar oscillating behavior of the ACF has also been observed in generic superlattices [39], carbon nanotubes [44], silica structures [45], and metal organic frameworks [46]. Initially attributed to relative oscillations of bonded atoms with different masses with respect to each other [47], it was later observed in materials containing only one species of atoms [48]. It has recently been shown [39] that these oscillations are due to zero wave vector

optical phonon modes. The Fourier transform of the heat flux ACF exhibited peaks in excellent agreement with the zero-**k** optical phonon normal modes computed by lattice dynamics. We find similar behavior in Na_xCoO_2, as shown in Figure 2 for the normalized ACF of three thicknesses of the $Na_{0.71}Co_{0.96}O_2$ supercell on a time scale of 2 ps. The inset (b) in Figure 2 shows the Fourier transform of the heat flux ACF, indicating a single optical phonon frequency of ν=23.8×10^{12} s^{-1}. However, the Γ-point optical phonons do not participate in heat flux since their contribution to the ACF integrates to zero over time, thus they do not contribute to the lattice thermal conductivity and the differences in optical phonon energies are insignificant for our purposes.

3.2 Size Scaling

As discussed above it is necessary to determine the convergence of κ_L with respect to the supercell size. For $Na_{0.71}Co_{0.96}O_2$, the two relevant thermal lattice thermal conductivities are in the *xy*-plane of CoO_2 layers and along the perpendicular *z*-direction, designated $\kappa_{\|}$ and κ_Z, respectively. In order to accurately model the scaling of κ_L from finite supercell to bulk, individual supercells are constructed so that all three dimensions are similar in length. Twelve supercells are constructed, ranging in length from 10 Å to 66 Å along the *x*- and *y*-axes and from 11 Å to 66 Å along the *z*-axis, with $\kappa_{\|}$ and κ_Z for each crystal calculated using the ensemble averages of the ACF integrals. The results of these calculations are presented in Figure 3.

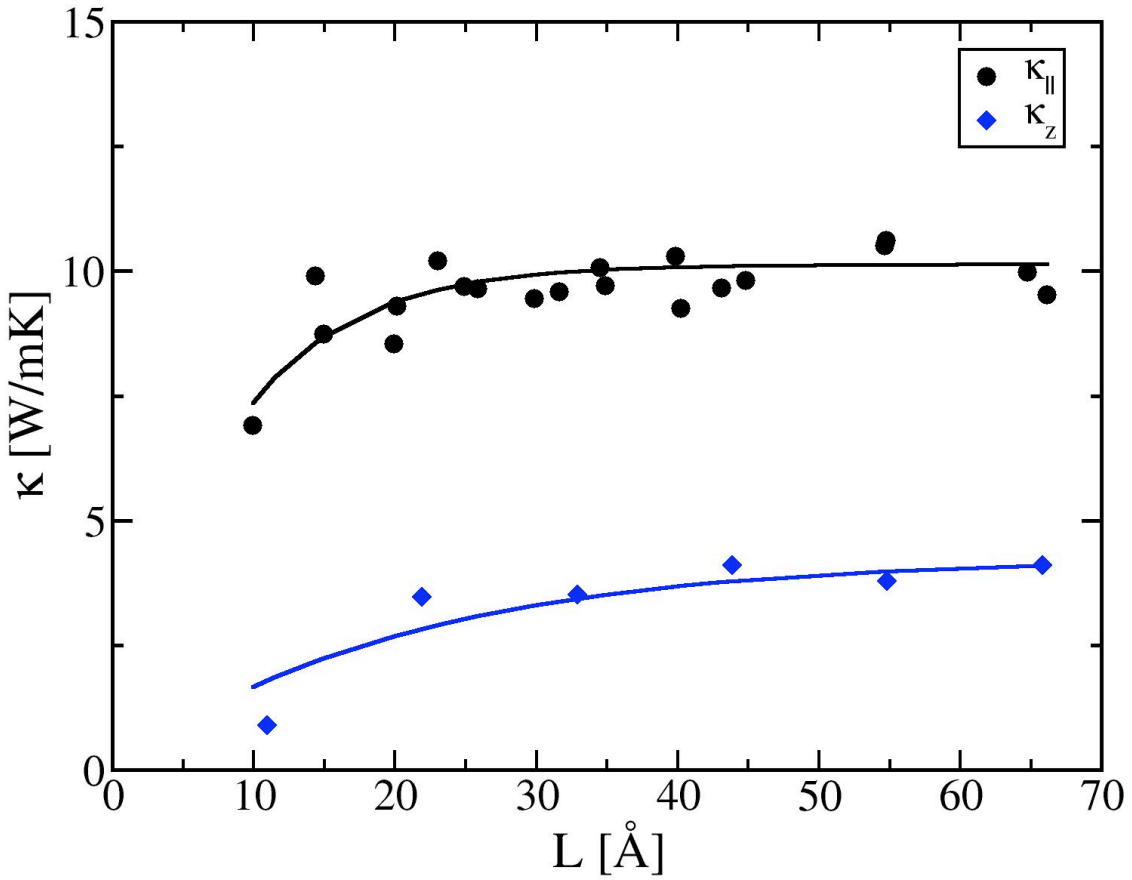

Fig. 3. (Color online) Lattice thermal conductivity computed for $Na_{0.71}Co_{0.96}O_2$ at room temperature in the in plane $\kappa_{\|}$ and out of plane κ_Z directions for the supercells sizes in the corresponding directions of heat propagation.

The bulk values of $\kappa_{\|}$ and κ_Z are approached asymptotically with increasing supercell size, leading to bulk thermal conductivity values $\kappa_{\|}$ = 10.1 W/mK and κ_Z = 4.26 W/mK. The bulk values are essentially achieved when the

supercell length in the direction of heat propagation reaches approximately 40 Å in each dimension, which is the basis for the choice of the orthogonal supercell with dimensions 39.2Å×39.64Å×43.5Å (6577 atoms) used in the calculations in the subsequent sections. Although these bulk values cannot yet be compared directly to the experiment for $Na_{0.71}Co_{0.96}O_2$ due to the difficulties in separating the lattice and electronic parts of thermal conductivity, the values we obtain for $Na_{0.5}CoO_2$ and $NaCoO_2$ show excellent agreement for $Na_{0.5}CoO_2$ and moderate agreement for $NaCoO_2$ with the results of the MD simulations obtained in Refs. (25, 27), as shown in Table 2. The excellent agreement regarding $Na_{0.5}CoO_2$ occurs since both studies constructed $Na_{0.5}CoO_2$ in the γ-phase, while the moderate agreement occurs regarding $NaCoO_2$ because the present study maintained the γ-phase while the Tada study constructed $NaCoO_2$ in the more stable (for that Na concentration) α-phase. Keeping $NaCoO_2$ in the γ-phase in the present study enables a determination of the effect of phase on thermal conductivity for $NaCoO_2$, in addition to singling out the influences of Na and Co-vacancy concentrations. The finding here is that an approximate decrease by 25% in thermal conductivity for $NaCoO_2$ occurs in both directions when the phase is changed from α to γ. The greater stability of the α-phase for $NaCoO_2$, as shown by its lower enthalpy of formation compared to the γ-phase [27], results in a tighter bound crystal that transfers heat more efficiently and therefore has increased thermal conductivity. This indicates that γ-phase Na_xCoO_2 is preferable for thermoelectric applications due to its lower κ_L.

TABLE 2. Comparison of thermal conductivities obtained for $Na_{0.5}CoO_2$ and $NaCoO_2$ [W/mK] between present study and results found in literature

Source	$Na_{0.5}CoO_2$		$NaCoO_2$	
	$k_{\|\|}$	k_z	$k_{\|\|}$	κ_z
MD simulation (present study)	20.8	4.8	30.1	13.1
MD simulation[a]	20.7	4.2	41.6	17.7

[a]Tada *et al.*[25,27]

3.3 Effects of Varying Concentrations and Temperature

The most efficient materials for constructing thermoelectric devices require a minimal value of the lattice thermal conductivity. Figure 4 (a) presents the results of the analysis in which Na concentration is varied from Na fraction x = 0.3 to 1.0, while keeping the Co fraction at 1.0 (no Co vacancies) at room temperature. The thermal conductivities increase monotonically to plateaus of approximately 20 W/mK at x = 0.5 for $\kappa_{\|}$ and approximately 6.5 W/mK at x = 0.71 for κ_z. The plateaus persist until about x = 0.8 for both κ's, and are followed by increases up to peak values at x = 1.0 of $\kappa_{\|}$ = 30.1 W/mK and κ_z = 13.1 W/mK. These are increases relative to the plateaus of about 50% for $\kappa_{\|}$ and about 100% for κ_z, respectively. The overall increase in thermal conductivity with increasing Na fraction is expected since Na vacancies enhance phonon scattering, thereby reducing thermal conductivity. Away from the extreme values of Na concentration, such as a low value of 0.3 and ideal 1.0, the lattice thermal conductivity is relatively weakly dependent on the amount of Na in the material. The relatively weak dependence of thermal transport on the Na concentrations within the middle range of Na ratios indicates that Na atoms located between CoO_2 layers have little direct effect on the in-plane phonon transport.

On the other hand, we find a relatively strong effect of κ_L as a function of Co vacancy concentration, which is varied from zero to 10% in Figure 4 (b). In ideal materials with no Co vacancies the peak values of lattice thermal conductivity are $\kappa_{\|}$ = 19.7 W/mK and κ_z = 7.0 W/mK. Introduction of Co vacancies leads to a significant decrease in κ_L. For example for experimentally observed concentrations of 4% in-plane $\kappa_{\|}$ is lowered by more than a factor of two, to 9.6 W/mK, and out-of-plane κ_z is lowered to 3.4 W/mK. Further increase in Co vacancies concentrations leads to decrease in lattice thermal conductivity to $\kappa_{\|}$ =5.6 W/mK and κ_z = 2.4 W/mK at 10% Co vacancy concentration. This behavior also suggests that the heat transport occurs within CoO_2 layers and introducing Co vacancies leads to a more significant scattering of in-plane acoustic phonons.

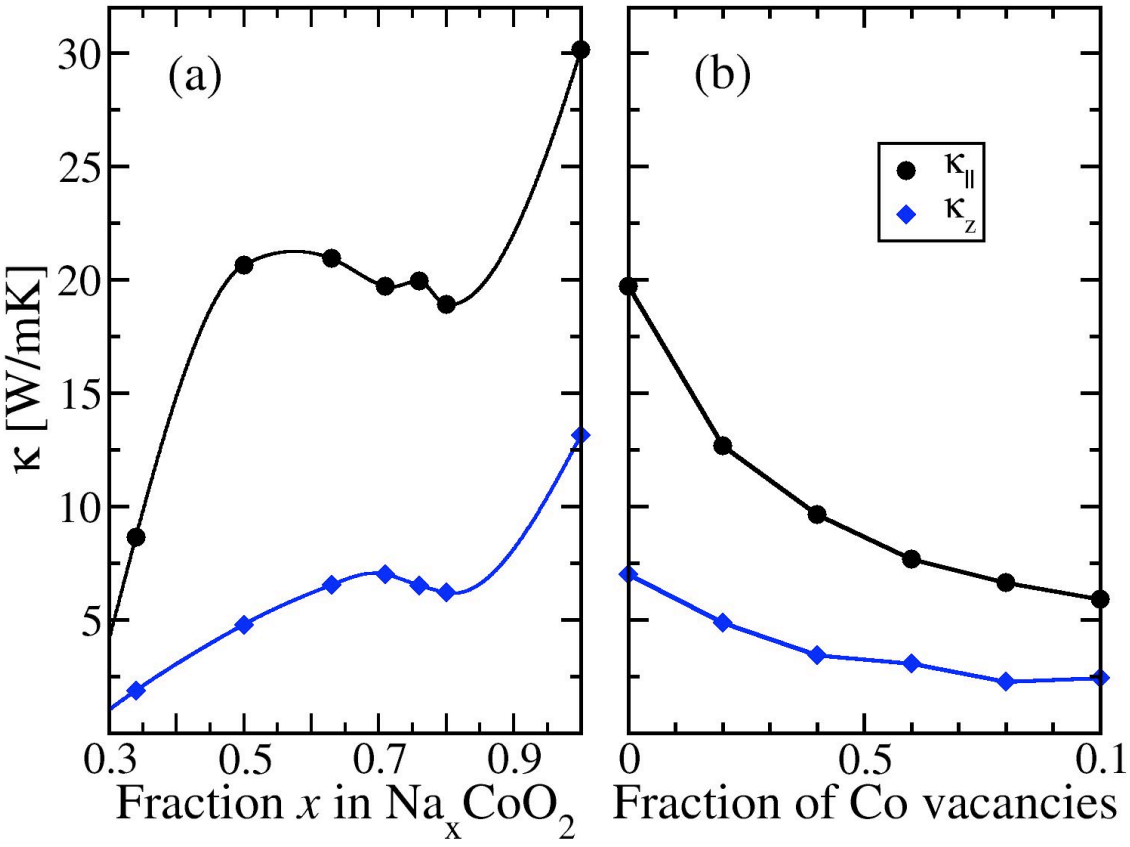

Fig. 4. (Color online) Room temperature lattice thermal conductivity of Na_xCoO_2 computed in plane $\kappa_{||}$ and out of plane κ_Z directions as a function of (a) fraction of Na x in the sample with no Co vacancies and (b) concentration of Co vacancies with fraction of Na x=0.7.

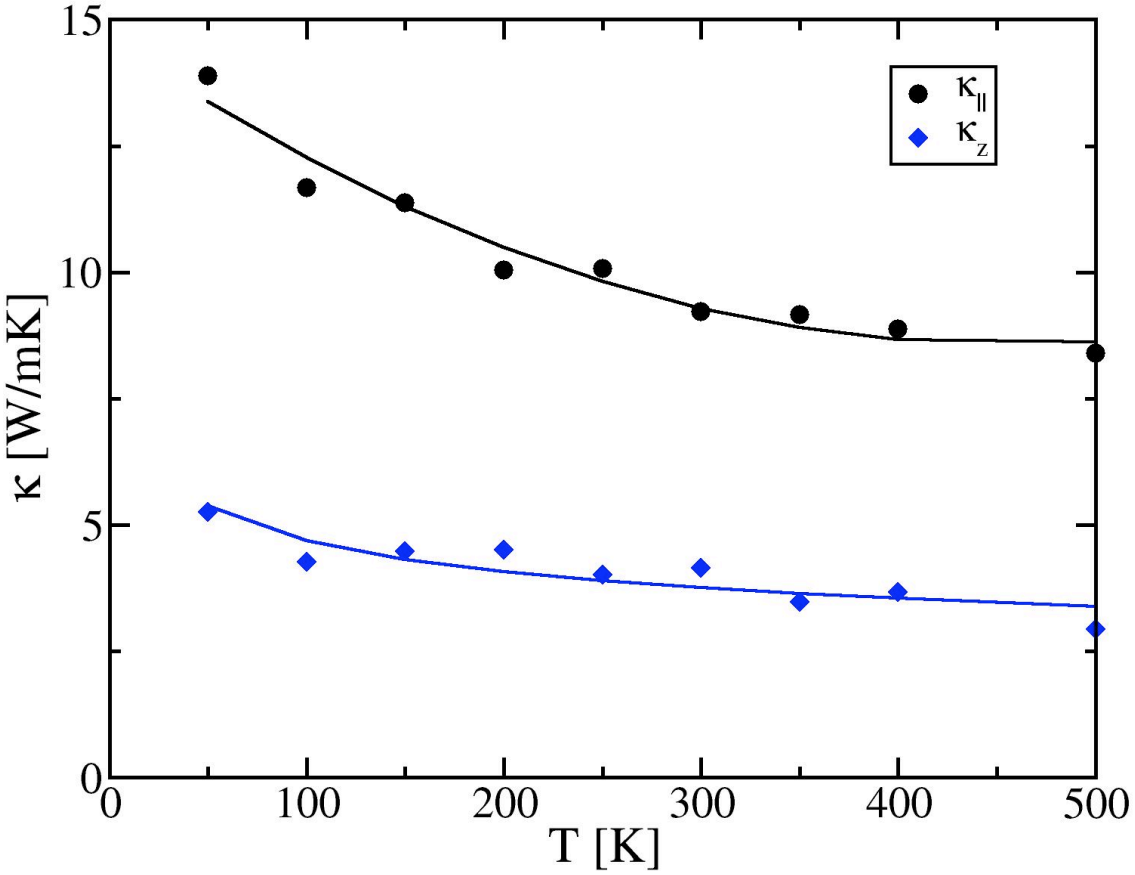

Fig. 5. (Color online) Lattice thermal conductivity of $Na_{0.71}Co_{0.96}O_2$ computed in plane $\kappa_{||}$ and out of plane κ_Z directions as a function of temperature.

Fig. 6 presents the results of the MD thermal conductivity calculations in which temperature is varied from 50 K to 500 K for $Na_{0.71}Co_{0.96}O_2$. The graph shows that kappa depends relatively weakly on temperature, dropping monotonically from peak values at the low temperature of 50 K ($\kappa_{||}$ = 13.9 W/mK and κ_z = 5.3 W/mK) to minimum values at the high temperature of 500 K ($\kappa_{||}$ = 8.4 W/mK and κ_z = 2.9 W/mK). As expected κ_L decreases with temperature because phonon-phonon scattering increases with rising temperature, thus reducing thermal conductivity. This implies that the thermoelectric figure of merit will increase with temperature due to two effects, i.e. dropping κ_L and increased thermopower [13].

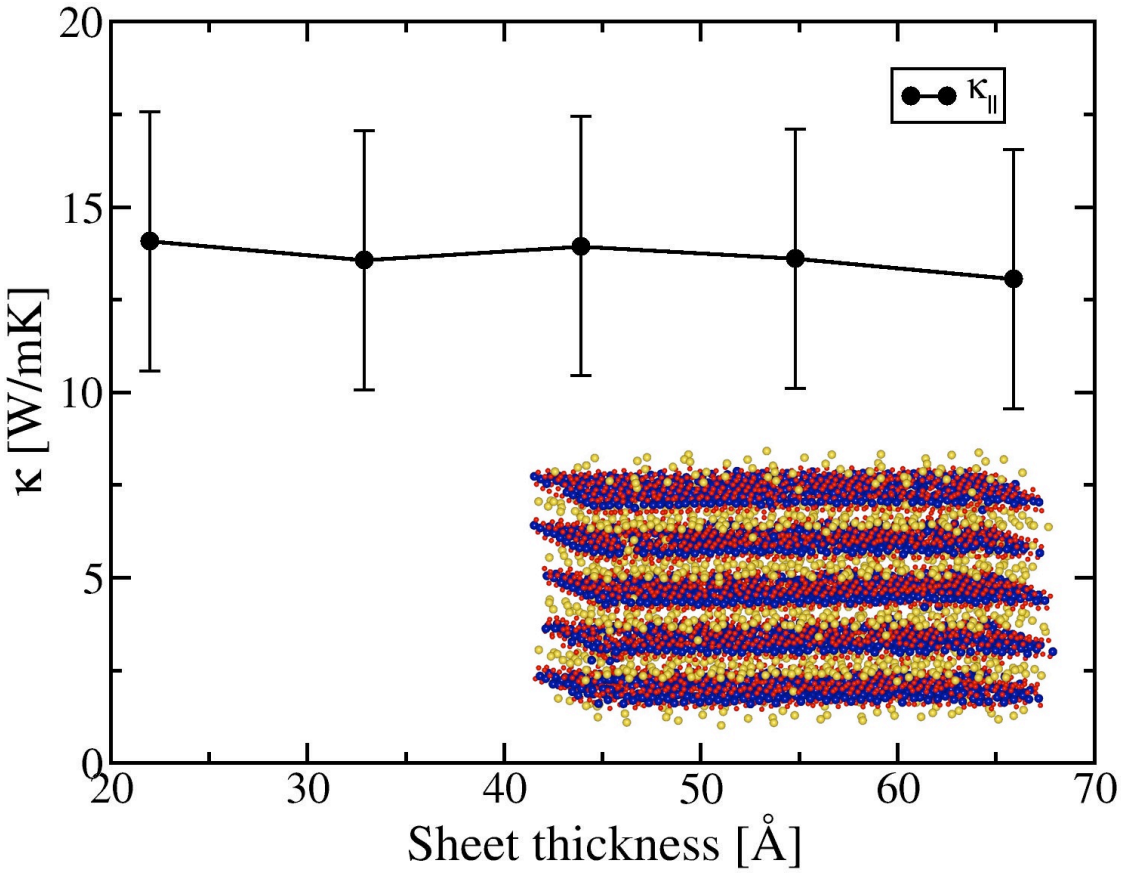

Fig. 6. In-plane lattice thermal conductivity $\kappa_{||}$ of $Na_{0.71}Co_{0.96}O_2$ nanosheets computed as a function nanosheet thickness at room temperature. The error bars indicate large fluctuations of $\kappa_{||}$ between the different ensembles. The inset shows the snapshot of atomic structure of the 22 Å nanosheet after 1.5 ns. Small red and blue atoms indicate oxygen and cobalt, respectively; larger orange atoms indicate Na.

3.4 Nanoscaling Effects

Recently efficient production of chemically exfoliated nanosheets of $Na_{0.71}Co_{0.96}O_2$ has been demonstrated [29]. The nanosheets have the potential to be used as the building blocks of future thermoelectric devices. The main idea is the reduction of lattice thermal conductivity due to enhanced phonon scattering by the nanosheet surface. Here we calculate the lattice thermal conductivity of several thicknesses of $Na_{0.71}Co_{0.96}O_2$ nanosheets and compare the nanoscaling effects with the obtained bulk data.

The nanosheets are constructed by introducing vacuum layers between $Na_{0.71}Co_{0.96}O_2$ slabs. The stoichiometry of the calculated nanosheets is kept close to those studied experimentally in Ref. 29, including the introduction of 4% of cobalt vacancies. Fixed boundary conditions in the *z*-direction are used while keeping periodic boundary conditions in the *xy* plane. The unphysical dipole interactions between the adjacent slabs are eliminated

following Ref. 49. Several thicknesses of nanosheets ranging from 22 Å to 66 Å are tested, containing from 3951 to 16924 atoms in order to probe phonon scattering effects. The surface consists of perfect O-terminated cobalt oxide with no surface roughness. Initially all Na atoms are located between CoO_2 sheets. However, during the statistics accumulation the structure snapshots reveal that Na atoms are highly mobile, readily diffusing to the surface (inset to Figure 6), thereby slightly decreasing the effective Na concentration in the nanosheets. Nanosheets calculations are also numerically challenging because the dynamics of the system and the ACF in particular are very sensitive to accurate enforcement of the charge neutrality conditions, and to a smaller extent the size scaling. In addition, the ensemble averaging becomes even more important since any run of a single nanosheet even for a relatively long time, such as 2 ns, normally results in the values of the in-plane lattice thermal conductivity varying by 3-4 W/mK from the ensemble average. This is illustrated in Figure 6, where ensemble average of $\kappa_{\parallel}$ is plotted as a function of the nanosheet thickness. The slightly inflated values of $\kappa_{\parallel}$ in comparison with the bulk value of 10.1 W/mK is most likely due to the effective lowering of the Na concentration as a result of Na atoms diffusing to the surface. As shown in Figure 4 (a), the decrease of Na fraction from 0.7 to around 0.5 leads to a slight increase of in-plane lattice thermal conductivity.

Most importantly, Figure 6 demonstrates insensitivity of the in-plane lattice thermal conductivity of $Na_{0.71}Co_{0.96}O_2$ nanosheets to the nanosheet thickness. Within calculated thickness range from 20 to 67 Å the computed $\kappa_{\parallel}$ remains practically constant at around 13.7 W/mK. This could be understood taking into account the fact that the CoO_2 sheets are very weakly coupled in Na_xCoO_2, suggesting that most of the heat flux responsible for the observed values of κ is propagating within nearly isolated CoO_2 layers. This behavior is also consistent with the anisotropy of bond strengths in Na_xCoO_2, and the computed anisotropy of lattice thermal conductivity in the bulk. This suggests that little enhancement in thermoelectricity of Na_xCoO_2 could be expected from nanoscaling only. For the same reason, introducing additional surface roughness to the nanosheets or bulk samples in order to limit the in-plane phonon transport would also likely result in limited improvement. A possible future direction of development of these materials is more likely in heavy atom doping, in order to enhance acoustic phonon scattering within CoO_2 layers.

Conclusions

In summary, using the Green-Kubo theory we have performed a detailed analysis of lattice thermal conductivity of Na_xCoO_2. We identify the nature of two competing mechanisms leading to a favorable scaling of Green-Kubo approach with respect to the supercell size. In smaller supercells these are the spurious correlations of the heat flux fluctuations and the decreased number of long wavelength phonon modes available for the heat transport. We find that within the medium values of Na fractions x (0.5-0.8), the lattice thermal conductivity weakly depends on the amount of Na in the material. This is due to the fact that acoustic phonons that transfer the heat are localized in CoO_2 layers, and Na atoms occupying the inter-layer space have limited influence on this transport. As a result bulk lattice thermal conductivity exhibits strong anisotropy, for example in $Na_{0.71}CoO_2$, is $\kappa_{\parallel}$ = 19.7 W/mK while κ_z = 7.0 W/mK at room temperature. Due to the same anisotropy the introduction of Co vacancies within the layers leads to a significant reduction in the in-plane lattice thermal conductivity $\kappa_{\parallel}$. For example, introducing 4% of Co vacancies leads to the reduction in lattice thermal conductivity by a factor of two, from 19.7 W/mK in $Na_{0.71}CoO_2$ to 9.6 W/mK in $Na_{0.71}Co_{0.96}O_2$. Further increase of Co vacancy concentration to 10% reduces the in-plane $\kappa_{\parallel}$ values to 5.6 W/mK. The in-plane lattice thermal conductivity in $Na_{0.71}Co_{0.96}O_2$ also decreases with temperature from 13.8 W/mK at 100K to 8.6 W/mK at 500 K. Finally, the effect of nanoscaling of Na_xCoO_2 is predicted to have a limited effect. The strong anisotropy in lattice properties also leads to a virtually constant calculated value of in-plane lattice thermal conductivity for the nanosheet thicknesses ranging from 20 to 67 Å. The decoupled nature of phonon transport within the CoO_2 sheets suggests that nanosheets even with artificially created surface roughness are likely to have thermoelectric properties similar to those of the bulk material. Therefore an alternative promising direction in improving thermoelectric performance of layered complex metal oxides could be in enhancing in-plane acoustic phonon scattering, for example by introducing heavy element doping.

Acknowledgements
This worked used the computational facilities of the VCU Center for High Performance Computing.

References

[1] J.-J. Braconnier, C. Delmas, C. Fouassier, P. Hagenmuller, Mater. Res. Bull. 15 (1980) 1797.

[2] C. Delmas, J.-J. Braconnier, C. Fouassier, P. Hagenmuller, Solid State Ionics 3 (1981) 165.
[3] K. Takada, H. Sakurai, E. Takayama-Muromachi, F. Izumi, R. Dilanian, T. Sasaki, Nature 422 (2003) 53.
[4] R. Schaak, T. Klimczuk, M. Foo, R. Cava, Nature 424 (2003) 527.
[5] I. Terasaki, Y. Sasago , K. Uchinokura, Phys. Rev. B 56 (1997) 75397.
[6] Y. Wang, N. S. Rodago, R. J. Cava, N. P. Ong, Nature 423 (2003) 425.
[7] T. Takeuchi, T. Kondo, T. Takami, H. Takahashi, H. Ikuta, U. Mizutani, K. Soda, R. Funahashi, M. Shikano, M. Mikami, S. Tsuda, T. Yokoya, S. Shin, T. Muro, Phys. Rev. B 69 (2004) 125410.
[8] H. J. Xiang, D. J. Singh, Phys. Rev. B 76 (2007) 195111.
[9] D. Qian, L. Wray, D. Hsieh, L. Viciu, R. J. Cava, J. L. Luo, D. Wu, N. L. Wang, M. Z. Hasan, Phys. Rev. Lett. 97 (2006) 186405.
[10] M. R. Peterson, B. S. Shastry, J. O. Haerter, Phys. Rev. B 76 (2007) 165118.
[11] W. Koshibae, K. Tsutsui, S. Maekawa, Phys. Rev. B 62 (2000) 6869.
[12] D. J. Singh, Phys. Rev. B 61 (2000) 78743.
[13] P. Wissgott, A. Toschi, H. Usui, K. Kuroki, K. Held, Phys. Rev. B 82 (2010) 201106.
[14] N. Hamada, T. Imai, H. Funashima. J Phys: Cond. Mat. 19 (2007) 365221.
[15] D. J. Singh, D. Kasinathan, J Electr. Mat. 36 (2007) 736.
[16] C. Fouassier, J. Matejka, J.-M. Reau, P. Hagenmuller, J. Solid State Phys. 6 (1973) 532.
[17] Y. Takahashi, Y. Gotoh, J. Akimoto, J Solid State Chem. 172 (2003) 22.
[18] J. W. Lynn, Q. Huang, C. M. Brown, V. L. Miller, M. L. Foo, R. E. Schaak, C. Y. Jones, E. A. Mackey, R. J. Cava, Phys. Rev. B 68 (2003) 214516.
[19] Q. Huang, M. L. Foo, R. A. Pascal, Jr., J. W. Lynn, B. H. Toby, Tao He, H. W. Zandbergen, R. J. Cava, Phys. Rev. B 70 (2004) 184110.
[20] L.Viciu, J. W. G. Bos, H. W. Zandbergen, Q. Huang, M. L. Foo, S. Ishiwata, A. P. Ramirez, M. Lee, N. P. Ong, R. J. Cava, Phys. Rev. B 73 (2006) 174104.
[21] L. Viciu, Q. Huang, R. J. Cava, Phys. Rev. B 73 (2006) 212107.
[22] Y. S. Meng, Y. Hinuma, G. Ceder, J Chem. Phys. 128 (2008) 104708.
[23] Z. Li, J. Yang, J. G. Hou, Q. Zhu, Phys. Rev. B 70 (2004) 144518.
[24] P. K. Jha, A. Tropera, I. C. da Cunha Limab, M. Talatic, S.P. Sanyal, Physica B: Cond. Mat. 366 (2005) 153.
[25] M. Tada, M. Yoshiya, H. Yasuda, J Elec. Mater. 39 (2010) 1439.
[26] M. Yoshiya, T. Okabayashi, M. Tada, C. A. J. Fisher, J Elec. Mater. 39 (2010) 1681.
[27] M. Tada, M. Yoshiya, H. Yasuda, Trans. Mater. Res. Soc. Japan 35 (2010) 205.
[28] Y. Masuda, Y. Hamada, W. S. Seo, K. Koumoto, J. Nanosci. Nanotech. 6 (2006) 1632.
[29] M. Aksit, D. P. Toledo, R. D. Robinson, J Mater. Chem. 22 (2012) 5936.
[30] K. Koumoto, Y. Wang, R. Zhang, A. Kosuga, R. Funahashieo, Ann. Rev. Mater. Res. 40 (2010) 363.
[31] M. S. Dresselhaus, G. Chen, M. Y. Tang, R. Yang, H. Lee, D. Wang, Z. Ren, J.-P. Fleurial, P. Gogna, Adv. Mater. 19 (2007) 1043.
[32] D. O Demchenko, P. D Heinz, B. H. Lee, Nanoscale Res. Lett. 6 (2011) 502.
[33] M. S. Green, J. Chem. Phys. 22 (1954) 398.
[34] R. Kubo, J. Phys. Soc. Jpn. 12 (1957) 570.
[35] S. Plimpton, J Comp. Phys. 117 (1995) 1.
[36] http://lammps.sandia.gov
[37] S. G. Volz, G. Chen, Phys. Rev. B 61 (2000) 2651.
[38] K. Esfarjani, G. Chen, H. T. Stokes, Phys. Rev. B 84 (2011) 085204.
[39] E. S. Landry, M. I. Hussein, A. J. H. McGaughey, Phys. Rev. B 77 (2008) 184302.
[40] X. W. Zhou, S. Aubry, R. E. Jones, A. Greenstein, P. K. Schelling, Phys. Rev. B 79 (2009) 115201.
[41] D. P. Sellan, E. S. Landry, J. E. Turney, A. J. H. McGaughey, C. H. Amon, Phys. Rev. B 81 (2010) 214305.
[42] M. Cherry, M. S. Islam, C. R. A. Catlow, J. Sol. Sta. Chem. 118 (1995) 125.
[43] T. Seetawan, V. Amornkitbamrung, T. Burinprakhon, S. Maensiri, K. Kurosaki, H. Muta, M. Uno, S. Yamanaka, J. All. Comp. 403 (2005) 308.
[44] Z. Yao, J.-S. Wang, B. Li, G.-R. Liu, Phys. Rev. B 71 (2005) 085417.
[45] A. J. H. McGaughey, M. Kaviany, Int. J. Heat Mass Tran. 47 (2004) 1799.
[46] B. L. Huang, A. J. H. McGaughey, M. Kaviany, Int. J Heat Mass Tran. 50 (2007) 393.
[47] J. Che, T. Cagin, W. Deng, W.A. Goddard III, J. Chem. Phys. 113 (2000) 6888.
[48] J. Dong, O.F. Sankey, C.W. Myles, Phys. Rev. Lett. 86 (2001) 2361.
[49] I. C. Yeh, M. L. Berkowitz, J. Chem. Phys. 111 (1999) 3155.